Conformational dynamics of mCherry variants: a link between sidechain motions and fluorescence brightness

Srijit Mukherjee [1, 2], Premashis Manna [3], Nancy Douglas [2], Prem P. Chapagain [4], and Ralph Jimenez [1, 2]

[1] JILA, University of Colorado, Boulder and National Institute of Standards and Technology, 440 UCB, Boulder, Colorado 80309, United States

[2] Department of Chemistry, University of Colorado, Boulder, 215 UCB, Boulder, Colorado 80309, United States

[3] Department of Chemistry, Massachusetts Institute of Technology, Cambridge, Massachusetts 02139, United States

[4] Department of Physics, Florida International University, 1200 SW 8th ST, CP204, Miami, FL 33199

KEYWORDS

Fluorescent Proteins, mCherry, Molecular Dynamics, Photophysics, Fluorescence

ABSTRACT

We recently developed the red fluorescent protein (RFP) mCherry-XL, which is threefold brighter than its predecessor, mCherry, with a directed evolution approach using fluorescence-lifetime flow cytometry selections. The enhanced brightness is due to a significant decrease in the non-radiative decay rate underlying its increase in fluorescence quantum yield. To examine the dynamic role of the four mutations that distinguish the two RFPs and closely-related variants, we employed microsecond-timescale, all-atom molecular dynamics simulations to sample their ground state conformational landscapes. The simulations revealed the significance of the I197R mutation, which leads to the formation of multiple hydrogen-bonded contacts. The triad of interactions observed between residues K70, E148 and 197R is also seen in mScarlet, another RFP of unrelated origin, but of comparably high brightness. These substitutions in mCherry-XL increased the rigidity of the β-barrel, for example as shown by increased hydrogen-bonding in the chromophore region and decreased root-mean-square backbone deviations. Furthermore, mCherry-XL showed significantly less ns-timescale breathing of the gap between β-7 and β-10 strands. This gap was

previously shown to be the most flexible region of mCherry, permitting entry of O_2 into the barrel. We also characterize the role played by the sidechain of residue 161 using a combination of MD simulations and in-vitro experimental characterization. We find this position is critical to the steric interactions that perturb the chromophore electronic structure. MD simulations also help us to recognize a network of hydrogen-bonded interactions between the chromophore, the residue 143, 163 and 59, which can potentially impact the electron distribution of the chromophore. Finally, we shed light on the conformational dynamics of the conserved residues R95 and S146, which are hydrogen bonded to the chromophore, and provide physical insights into the observed photophysics. To the best of our knowledge, this is the first study that evaluates the conformational space for a set of closely related FPs generated by directed evolution.

Introduction

The discovery and subsequent development of fluorescent proteins (FPs) have revolutionized biological imaging.[1-5] FPs are also being employed in a wide range of modern technological applications, from polymer-embedded emitters for bio-hybrid LEDs to edible fluorescent silk tags for on-dose authentication of pills to combat counterfeit medications.[6, 7] This broad utility has led to the development and tailoring of FPs for highly specialized applications. For example, the green FP (GFP) mGreenLantern was exclusively engineered for high protein expression in neurons.[8] Efforts to develop highly expressing, fast maturing, bright and photostable FPs continue, as no single fluorophore can be optimal for all applications. [9] Though engineering based on de-novo design or site-directed and random mutagenesis has led to the development of several exceptionally bright FPs, with fluorescence quantum yields above 70%, such as mTurquoise2, mNeonGreen and mScarlet, there is often limited insight into structural dynamics that could potentially be used to tune the photophysics.[9]

Typically, the FP development pipeline comprises the generation of mutant libraries with site-directed or random mutagenesis of the templates, followed by high-throughput screening of fluorescence intensities or

fluorescence lifetime and further mutagenesis.[9-14] While hundreds of atomic-scale resolution X-ray crystal structures are available to guide library design, they only provide a snapshot of a small region of conformational space at low temperatures.[15, 16] In contrast, most applications employ FPs at room or physiological temperatures, thereby allowing the protein molecules many other conformational degrees of freedom which dictate its function.[16, 17] Nuclear Magnetic Resonance (NMR) methods are a powerful approach for sampling the conformational landscape of proteins at room temperature, but few NMR-based studies have been performed on FPs to date.[17, 18]

The structure and dynamics of the chromophore environment are obviously critical for controlling ultrafast dynamics which lead to nonradiative decay of the excited state, thus limiting the fluorescence quantum yield, but a clear picture is still emerging.[19-23] In most bright red FPs (RFPs), the chromophore occupies a cis-phenolate conformation in the ground state with the phenolate exhibiting a single-bond character and the negative charge localized on the O atom of the phenol moiety.[24, 25] Many recent studies have identified the rotation of the chromophore's P-bond as a primary pathway of ultrafast non-radiative decay.[9, 26-32] For example, Drobhizev and co-workers illustrated the roles of several sidechains in proximity of the MYG-chromophore in mCherry-like proteins in restricting the ability of the chromophore to access twisted intramolecular charge transfer (TICT) states through phenolate-bond (P-Bond) rotation.[29] The presence of these TICT states permits ultrafast non-radiative decay through a conical intersection seam on the excited-state surface. A high resolution (~1.5Å) crystal structure of mScarlet revealed that the sidechain of R197 (numbered with respect to mCherry) is central to the formation of a "cobweb" of hydrogen-bonds, which appears to restrict the chromophore flexibility. [33] This residue is generally found to be aliphatic in related RFPs such as the mFruit series. [2]

Beyond these experimental tools, there are in-silico methods for exploring protein structure and dynamics, such as ab-initio quantum mechanical calculations, force-field based classical molecular dynamics (MD) simulations and hybrid methods.[34, 35] While ab-initio quantum mechanics and dynamics simulations are

capable of simulating protein-chromophore interactions on ground and excited electronic states, they are currently limited to exploring picosecond timescales dynamics with implicit solvent models and are often challenged by the extensive configurational sampling required to obtain a proper representation of solvent and thermal effects for ~100-1000 atoms.[36] For example, Coppola et al. utilized ab-initio MD (AIMD) to sample the ground state surface of the entire avGFP protein (PDB: 1GFL) in the picosecond timescales and observed that several motions near the FP chromophore pocket are interlinked.[37] In particular, it was seen that motions for the N-atom on H148 and the phenolic O-atom on the chromophore were interlinked with the carbonyl on O-atom on the imidazolinone ring of the chromophore and the N-atom on the R96 residue of avGFP.[37] Many of these interactions were previously considered to be irrelevant in the hydrogen-bonded equilibrium for the A (protonated), I (intermediate deprotonated) and B (anionic) forms of the chromophore ground electronic state.[37] Although these insights are valuable, until new platforms such as quantum computers emerge, investigations will be limited to tracking dynamics of small subsets of the system on very short time scales.[38] Among the most widely-available computational tools, classical algorithms such as all-atom MD can greatly enhance understanding of the conformational space for large, explicitly-solvated molecules such as proteins or nucleic acids.[39, 40] For example, Graphical Processing Unit (GPU)-accelerated equilibrium MD simulations on long timescales (1–2 μs) have recently been used to follow the opening of tetrameric glutamate receptor ion channels in response to glutamate binding.[41] Analysis of generated trajectories provide a framework for exploring the electronic and steric effects on timescales beyond the excited-state lifetime, which may result from the conformational diversity of the chromophore environment. These studies can add dimension to our understanding of static models as, for example, Lin et al. gained insight into how the photophysical properties of the anionic GFP chromophore are modulated by electron-donating and -withdrawing substituents near the phenol and the imidazolinone ends.[23] Despite excellent functionality of their model for explaining photophysics of GFPs, it does not consider dynamics. Furthermore, there have been few attempts to extend this model to red or cyan FPs, which have electronic configurations different from most GFPs. All-atom classical MD simulations are thus a first step in

identifying the motions that impact FP photophysics and corelate conformational freedoms of sidechains to such static models.

We recently-developed bright FPs, such as FusionRed-MQV and mCherry-XL using high-throughput microfluidic fluorescence lifetime selections, both of which are ~3x higher molecular brightness than their parents FusionRed and mCherry, respectively.[12, 42,43] In this study, we focus on mCherry-XL, where we investigate the role and the chemical nature of the substitutions that were acquired in the course of its development using all atom MD simulations. In the photophysical analysis of mCherry-XL, we found the bulk of improvement in the fluorescence quantum yield came from the suppression of non-radiative rate, which was beyond the scope of an energy gap law.[42] The chemical nature of the point mutations acquired in the development of mCherry-XL agreed with the model of electron flow by Lin et.al.[23] In this study, we provide a structural framework, from the dynamic point of view, for these substitutions acquired in mCherry-XL and several of the intermediate mutants. We also provide a direct comparison with mScarlet—the brightest RFP described to date.[33] Similar to Coppola et al.,[37] we find interconnected dynamics of several amino acid residues, which can influence steric and electrostatic contributions to the electron structure of the FP chromophore, manifesting in the enhancement of brightness observed for mCherry-XL and mScarlet.

Methods and Materials:

Experimental: Supplementary Information Section S2 describes our protocols for cell growth and protein expression. In short, mCherry variants generated using fluorescence lifetime selections in yeast (*Saccharomyces cerevisiae* BY4741; transformed with the pYestDest52 vector) from our previous study were cloned into the pBad-His+ vector for bacterial expression. [12, 42, 43] Protein was extracted from bacteria using Ni-NTA-based column chromatography. Absorption data was collected using a Cary 5000 UV−vis near-IR spectrophotometer in the double beam mode. The emission and excitation data were collected using a HORIBA Jobin Yvon Fluorolog-3 FL3-222 instrument. Fluorescence lifetime data was collected using a

commercial time-correlated single photon counting (TCSPC) system (Fluoro-time 100, PicoQuant). The instrument was operated with a 560 nm pulsed laser diode head excitation source and a repetition rate of 5 MHz. An emission filter centered at 600 nm (60 nm FWHM) was used to filter the excitation and scattered photons. We provide the details of the fit and the instrument response function in Supplementary Information Section S3. All measurements were carried out with purified proteins diluted in Tris-HCl Buffer (pH ~7.4) to attain optical densities (ODs) of ~0.1 and ensure measurements were within the linear regime of the instrument response.

Computational: Explicit solvent, all-atom simulations were performed using the NAMD3.0 molecular dynamics package with the CHARMM36 force field.[44, 45] The initial X-ray crystallographic structures of mCherry and mScarlet were obtained from the Protein Data Bank (mCherry – PDB: 2H5Q, mScarlet – PDB: 5LK4) and the missing residues were inserted using MODELLER. Initial structures of variants were obtained using the Visual Molecular Dynamics (VMD) psfgen 2.0 plugin.[46] Force field parameters for the deprotonated, anionic form of the mature chromophore in the ground state were used, following previous work.[47, 48] The E215 residue was protonated using a patch. The VMD package was used to set up the system for simulations.[46] The initial structures were solvated with box padding of 12 Å, which resulted in a typical simulation box of dimensions 60×87×82 Å (typically ~40,000 atoms), depending on the variant. Each solvated system was electrically neutralized by randomly adding K+ ions to the system, along with 100 mM KCl. The particle mesh Ewald method was used to treat long-range interactions with a 12 Å nonbonded cutoff. A 4 ps energy minimization was performed using the conjugate gradient and line search algorithm. The system was then heated for 240 ps with a linear gradient of 1 K/ps from 60 to 300 K. At 300 K, each system was equilibrated for 2 ns with a 2 fs integration time step in the NVT ensemble, followed by a 2000 ns production run using NVT dynamics with 2 fs time steps. Langevin dynamics was used to maintain the temperature at 300 K. The VMD package was used for aligning the saved coordinates of each frame of the trajectories to the initial co-ordinates of the FP chromophore. RMSD, distance and angle calculations were calculated by utilizing short scripts (scripts modified from freely available codes in the GitHub repository:

https://github.com/ipudu) on the TkCon plugin of VMD. [46] RMSD for the protein backbone for each FP aligned with the first frame and the average structure is presented in Supplementary Information Table S5.1.

Results and Discussion:

a. Photophysical measurements and amino acid sequences

The mCherry variants investigated here were developed using lifetime-based microfluidic cell sorting of libraries constructed using site-directed and error-prone mutagenesis.[42] The photophysical properties were found to be sensitive to substitutions at positions 143, 161, 163 and 197 on the mCherry scaffold. These residues are located near the phenol end of the chromophore (Table 1). FPs with the I197R substitution display increased lifetime (1.5–2.5-fold higher than mCherry), larger Stokes shifts (>800 cm^{-1} vs. ~600 cm^{-1} observed for mCherry) and blue-shifted absorption and emission compared to mCherry (Supplementary Table S3.1). We also characterized mScarlet, which contains an Arg at position 197, but is otherwise unrelated to mCherry since it was derived from a synthetic template. **Error! Bookmark not defined.** Photophysical data are provided in Supplementary Table S3.1.

Table 1: Variation of amino acids at positions 143, 161, 163 and 197 on these FPs.

Protein	143	161	163	197
mCherry	W	I	Q	I
C12-3	I	C	L	R
C12-7	W	A	V	R
C12-8	M	S	I	R
mCherry-XL	S	V	Y	R
mScarlet	W	I	M	R

As observed previously,[42] the quantum yield scales with lifetime (Figure 1). The increase in the quantum yield correlates with progressive increases in the time constant corresponding to the major amplitude component of the fit and the fraction of this component in the overall fit (Supplemental Figure S3.3). This

trend towards a single-exponential fluorescence decay potentially indicates that brighter variants show reduced conformational heterogeneity.[49]

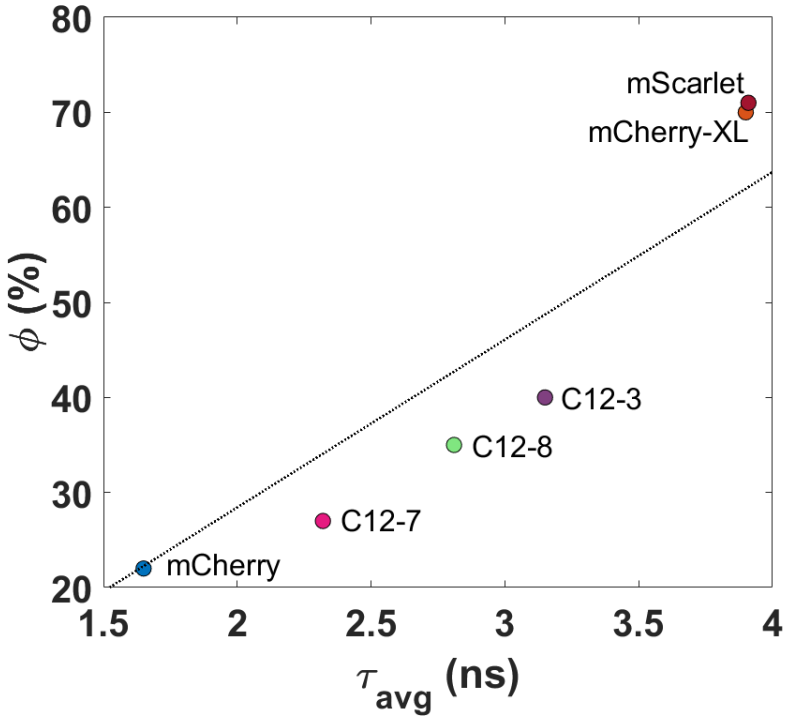

Figure 1: The linear scaling of fluorescence quantum yield with average intensity weighted fluorescence lifetime

b. Fluctuations and the rigidity of the β-barrel

Previous investigations of the interstrand dynamics of β7, β8 and β10 in mCherry revealed ns-timescale fluctuations of the gap between strands β7 and β10 as quantified by the distance between the α-C of residues A145 and K198 (Figure 2 and SI Figure S4.1).[47, 48] This region of the barrel was identified as an entry point for O_2 diffusion into the barrel. [47, 48] Reducing the amplitude of these interstrand dynamics was the goal in the library design of ~144,000 variants that led to the development of the photostable FP Kriek.[50] Interstrand dynamics can additionally reflect the rigidity of the FP barrel, which influences photophysical characteristics such as the Stokes shift and brightness.[9] Our simulations on mCherry are consistent with previous findings that the β7 and β10 strands fluctuate between open and closed conformations on ns

timescales (Figure 2 and SI Figure S4.1).[47, 48] Interestingly, these fluctuations are absent for mCherry variants with the I197R substitution, consistent with a strong I197R–E148 interaction, (discussed in the next subsection) where the residues 197 and 148 lie on β7 and β10, respectively. mCherry-XL, C12-3, and C12-8 primarily exhibit a major closed conformation (~4.5 Å), whereas C12-7 and mScarlet exhibit an open conformation (~7.5 Å) (Figure 2 and SI Section S4). Moreover, it should be emphasized, as in the case of the photostable RFP Kriek, the improvement of photostability could be attributed to a combination of two factors – a 2-fold reduction in lifetime that could improve photostability by 50% under confocal illumination (and 80% under widefield illumination) and the reduction of O_2 diffusion into the barrel through the effective reduction of the β7-β10 fluctuation.[50] Based on this observation and according to our previous report, the quantum yield of photostability of mCherry-XL was 1.7-fold lower than that of mCherry under an excitation normalized irradiation of 10 W/cm^2, but the fluorescence lifetime was 2.5-fold higher.[42] This non-linear scaling of fluorescence lifetime with the photostability may indicate that the reduction of fluctuation between β7 and β10 strands impacts the diffusivity of O_2 in the β-barrel, hence protecting the chromophore from photodegradation for mCherry-XL, in comparison to mCherry.

To further assess the rigidity of the β-barrel, we also quantified the root mean square deviation of the backbone atoms for these FPs, and, brighter FPs (mScarlet and mCherry-XL) with reduced intrastrand dynamics, exhibit up to 1.2-1.8-fold lower values of RMSD than the dimmer FPs in this series (Supplementary Information S5b). Brighter FPs (mCherry-XL and mScarlet) on an average also exhibit a ~1.2-fold larger number of hydrogen-bonds in comparison to dimmer variants (e.g. mCherry) formed by the chromophore with nearby residues – indicating a conformationally restricted chromophore through direct interactions with the sidechain residues on the barrel (Supplementary Information S5c).

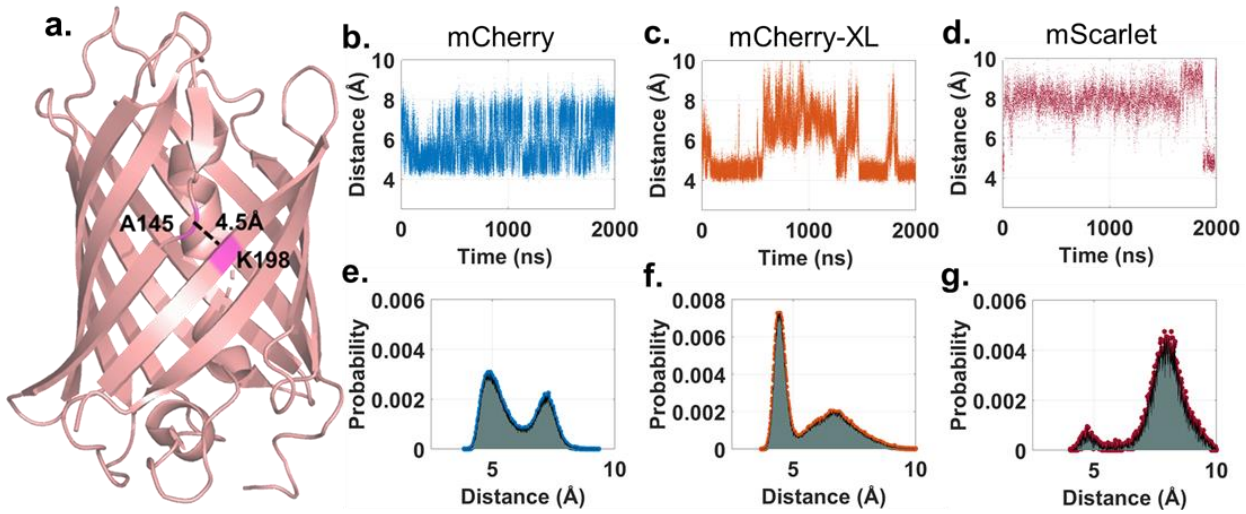

Figure 2: a. The locations of A145 and K198 in the structure of mCherry (PDB ID:2H5Q). (b-g). The distance–time trajectories and the normalized distance histograms for the spacing between the α-C on A145 and K198 for mCherry (blue), mCherry-XL (orange) and, mScarlet (maroon). The ~10s of ns-timescale fluctuations in mCherry which reflect the opening and closing of the gap between the strands β7 and β10 (panels b and e), are substantially reduced for mCherry-XL (panels c and f) and mScarlet (panels d and g).

c. Interactions of the Arg197 sidechain reduce β-barrel fluctuations

To further investigate the role of the sidechain at position 197 and its connection to a rigid barrel, we observe mCherry variants with Arg at position 197 also exhibit blue-shifted absorption and emission profiles with increased fluorescence lifetimes (Table S3.1). This is expected from the electron-withdrawing nature of a positively charged Arg residue near the phenol end of the chromophore, consistent with the static electro-optical model for the GFP chromophore developed by Lin and co-workers.[23] However, the dynamic role of this R197 residue remains unexplored, and on closer inspection of the MD trajectories, it indeed forms several long-lived interactions. These observations support steady-state crystal structure data for mScarlet, where MD simulations show that R197 exhibits several conformational states, each capable of interacting with the electron density of the π-cloud on the phenol ring. What stands out in one of the many interactions of this residue is a triad of hydrogen bonded interactions formed through the carboxylic

group of E148 and the amine groups of K/R70 for mCherry-XL and mScarlet, respectively. Figure 3 shows the nature of interactions and several conformational states seen for MD trajectories of mCherry, mCherry-XL and mScarlet (R70); the latter two forming specific long-lived conformations through a network of hydrogen bonds. These interactions are also present for the mCherry C12-X variants and are presented in the SI Section S6. The interactions are located on three spatially-distant regions of the FP molecule, where R197 is located on the β7 strand, E148 on β10 and the K/R70 on the α-Helix. For mCherry, the distance between K70 and I197 indicates the absence of long-lived conformational states, owing to the aliphatic nature of the Ile residue. In mCherry-XL, three distinct conformational states are seen at ~3 Å, 4.5 Å and 5.5 Å, which correspond to the distance measured between hydrogen atoms on K70 and R197. The first conformer indicates a direct hydrogen bond between two residues, while others indicate other hydrogen atoms on other amine groups on R197 and K70 and possible water-mediated and direct interactions. The mScarlet trajectory shows similar interactions, where the distance between the hydrogen atoms on R70 and R197 indicates two distinct conformational states, 3 Å and 6 Å, primarily due to the direct hydrogen bonds formed between the four possible combinations of amine groups available for the Arg–Arg interactions. (SI Figure S6.1)

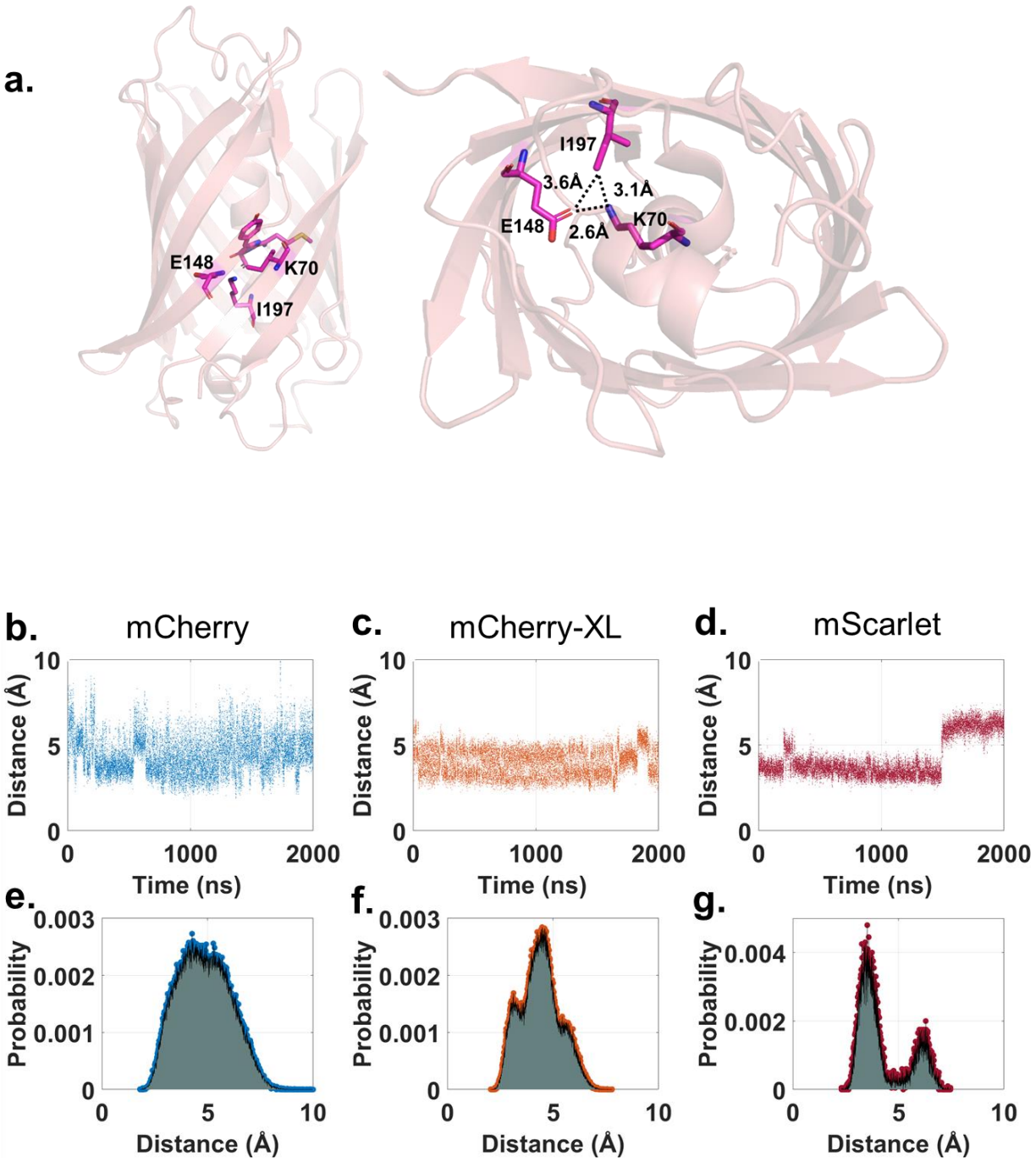
a.
E148
K70
I197
I197
3.6Å
3.1Å
E148
2.6Å
K70
b.
mCherry
c.
mCherry-XL
d.
mScarlet
Distance (Å)
Time (ns)
e.
f.
g.
Probability
Distance (Å)

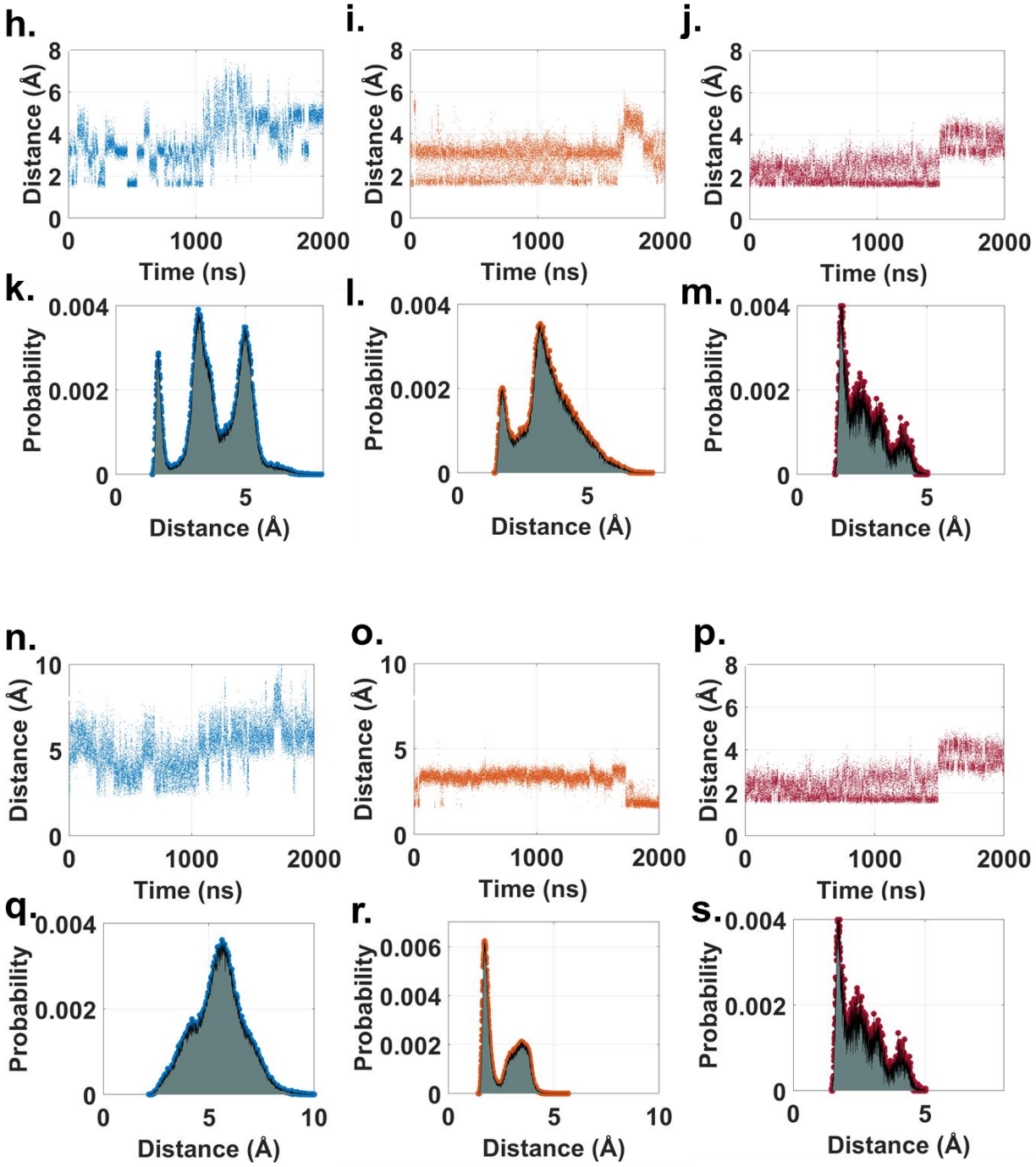

Figure 3: a. The location of the **148–197–70** triad on the mCherry structure (PDB ID:2H5Q) along with measured distances. (b-s) The distance–time trajectories and the area-normalized histograms indicating probabilities of sidechain conformations (b-g). **70–197** (h-m). **70–148** and (n-s). **148–197** in mCherry (blue), mCherry-XL (orange) and,

mScarlet (maroon), respectively. mCherry lacks the contacts between R197 and K/R70 and E148 seen in mCherry-XL and mScarlet.

The 148–197–70 interactions also restrict the mobility of K70, which is known to influence spectral blue shifts and brighten RFPs of the DsRed family.[51] In particular, Shu et al. used crystal structure data from the mFruits RFP family to demonstrate that the conformational freedom of K70 could explain the basis of spectral changes in these FPs.[51] Their findings indicated that the K83L (on the turn region of the barrel) substitution in mCherry (and mStrawberry), as opposed to the brighter and blue-shifted DsRed (and mOrange), was responsible for lowering the effective electrostatic repulsion between positively charged K83 and K70 residues on the protein α-Helix.[51] This resulted in an increase of the distance between the amine functionality on K70 and the electron cloud on the chromophore for the dimmer red-shifted mCherry (and mStrawberry). Similar observations were also noted using QM/MM simulations, where in-silico mutagenesis on the R70 residue of TagRFP-T revealed that positively charged electron withdrawing substituents result in the brightest, and the most blue-shifted variants (Quantum yield ratios of variants; ϕ_{R70}: ϕ_{K70}: ϕ_{A70}: ϕ_{Q70} = 4:3:2:6). [52] While Shu et al. reported an interlinked conformational change of K70 and L83 that reorients K70 towards the electron cloud of the chromophore, we find strong interactions in the E148–K70–R197 triad to be responsible for re-orienting K70 to a form seen in DsRed. The proximity of K70 to the electron cloud of the chromophore can participate in electrostatic effects absent in mCherry (Supplementary Information Figure S7.1 and S7.2). This is corroborated by the observation that a direct hydrogen-bond between the chromophore and K70 is observed for for only 7% of the structures recorded for the entire length of the trajectory, when compared to 34 % in mCherry-XL and 73% for mScarlet. (Supplementary Table S5.2)

Further investigation for this interaction reveals that mCherry exhibits three conformational states for K70, which can be quantified using the measured distance between the methine carbon (CB2) on the chromophore and the N-atom (NZ) of the primary amine on K70. The probabilities of conformations with

measured distances of ~ 4.5 Å, 5.5 Å and, 7 Å occur in a 2:1:2 ratio, and these conformers exhibit rapid ns timescale conformational switching. The third conformation (~7 Å), is populated for only 20% of the trajectory in mCherry-XL, thus reducing the distance between the chromophore and K70 to result in a more DsRed- or mOrange-like geometry.[51] This is also observed for mScarlet, where we use the distance between the N1 atom on R70 and the methine carbon. The abovementioned three possible distances for the C–N separation were also seen in mScarlet, with the 7 Å conformation accounting for even lower fractions (~10%) in this case. The trajectories and distance histograms are provided in the Supplementary Information Figure S7.1. From an electrostatic point of view, the residue K70, like R197, is a positively charged electron withdrawing group and can restrict the flow of electrons in excited-state charge transfer for the P-Bond flip pathway, to blue-shift and brighten dim RFPs like mCherry, as noted in this case.

d. Disruption of the 143–163–Chromophore interactions and the role of residue 161

We now turn our attention to other residues that were substituted in mCherry during the development of mCherry-XL. Residues at positions 143, 161 and 163 can directly interact with the FP chromophore (Figures 4 and SI Figure S9.1), impacting electron flow between the chromophore rings and potentially opening up non-radiative pathways for emission, leading to the increase of the major time constant in the fits of the fluorescence lifetime trace.[9] First, the mFruit family of FPs display a diverse range of amino acid substitutions at position 163.[53] Brighter, blue-shifted variants such as DsRed and mApple have a positively charged Lys residue at 163, capable of stabilizing the negatively charged phenolate moiety.[54] The possible electrostatic interaction can thus reduce the propensity for excited-state photoisomerization coupled to a P-to-I charge transfer process, brightening and blue-shifting the electronic transition energy of the chromophore.[29] Moreover, the residue at 163 also impacts the photostability of an FP. Regmi et al. used explicit oxygen sampling MD simulations to identify the role of the residue 163 in the photostability of mCherry variants. Based on their findings, the introduction of the M163Q substitution in mCherry with respect to its parent DsRed, is responsible for filling a cavity crucial to the O_2 diffusion pathway that leads

to photodegradation of the chromophore.[48] These residues were also mutated in our efforts to develop the photostable mCherry variant Kriek (mCherry W143I, I161M and Q163V).[50] Though, Kriek displayed ~3-fold higher photostability, it was red-shifted by ~5 nm in absorbance and emission and showed a ~3-fold lower fluorescence quantum yield.[50] It can thus be hypothesized that the introduction of several aliphatic groups of varying sizes can potentially disrupt favorable electrostatic interactions, leading to unfavorable impacts on brightness, but possibly positive impacts on photostability.[50] Similarly, mScarlet-H, which is a two-fold more photostable variant of mScarlet, has a single point mutation M163H.**Error! Bookmark not defined.** The higher photostability and a ~18 nm blue shift of the absorption and emission spectra with the substitution of an aliphatic residue with a positively charged sidechain at position 163 is consistent with observations on DsRed and Kriek.[50, 51]

In our efforts to evaluate the role of the sidechain at 163 in the crystal structure and the MD trajectories of mCherry, it appears that the amine moiety of Q163 interacts with the phenol moiety of the chromophore (Figure 4a, b and d). While uncharged, amine groups are electron rich and can explain the red-shift of variants such as mCherry. Moreover, Q163 in mCherry is tethered to this fixed orientation through a secondary interaction of Q163 with the W143 residue (carbonyl- π-cloud; Figure 4a, c and e). The sidechain at position 143, though surrounded by aliphatic residues on all sides on the barrel (L198 on β-10; A145 and M141 on β-7; and L165 on β-8) can interact with the backbone carbonyl group of D59 and the hydroxy group of S62 on the α-helix, as observed in mCherry's crystal structure. (Figure 4a) This results in a stabilizing network of interactions between the α-helix, W143, Q163, and the chromophore. Additionally, the static picture from the crystal structure also indicates that this interaction "pulls" the mCherry chromophore downwards, counteracting the "planarity", which is usually associated with brighter FPs. [9] However, this extensive hydrogen-bond network is notably altered in mCherry-XL and other variants of the C12 family. In mCherry-XL the Q163Y substitution initiates an interaction with the backbone carbonyl group of D59, whereas the smaller W143S does not (Figure 4j and k). This results in the orientation of the phenol residue of Y163 downward, hydrogen bonded to the backbone carbonyl of D59 (Figure 4l and m).

This orientation leads to a minimal interaction of Y163 and the chromophore, where breaking a direct interaction with the chromophore leads to a brighter FP. In mCherry-XL the combination of this effect with the strong upward pull of the chromophore by R197 results in a chromophore that may be significantly more planar than that of mCherry (Supplementary Information Section S10). X-ray crystallography can shed further light on chromophore planarity in mCherry-XL in comparison to mCherry and mScarlet.

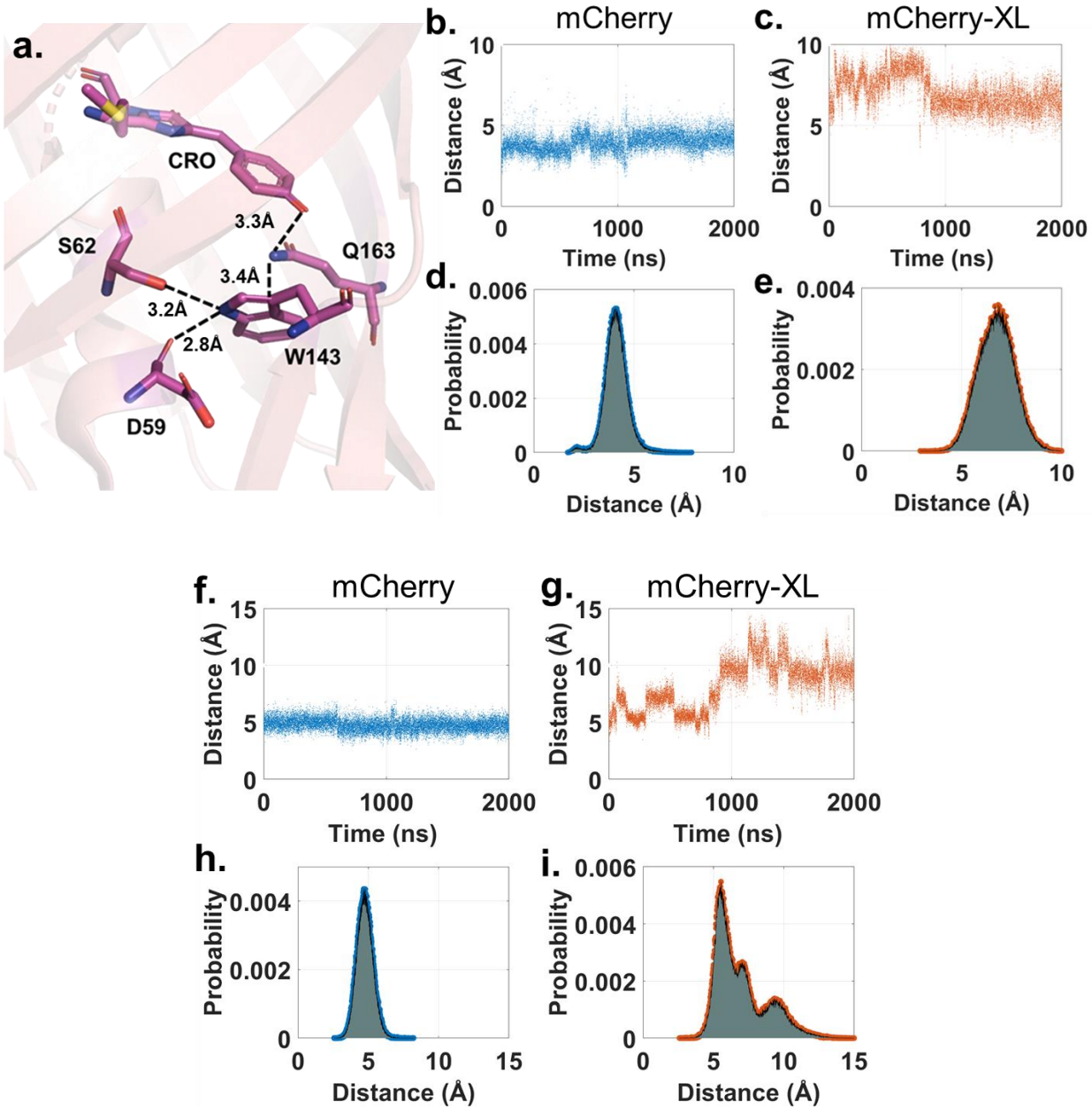

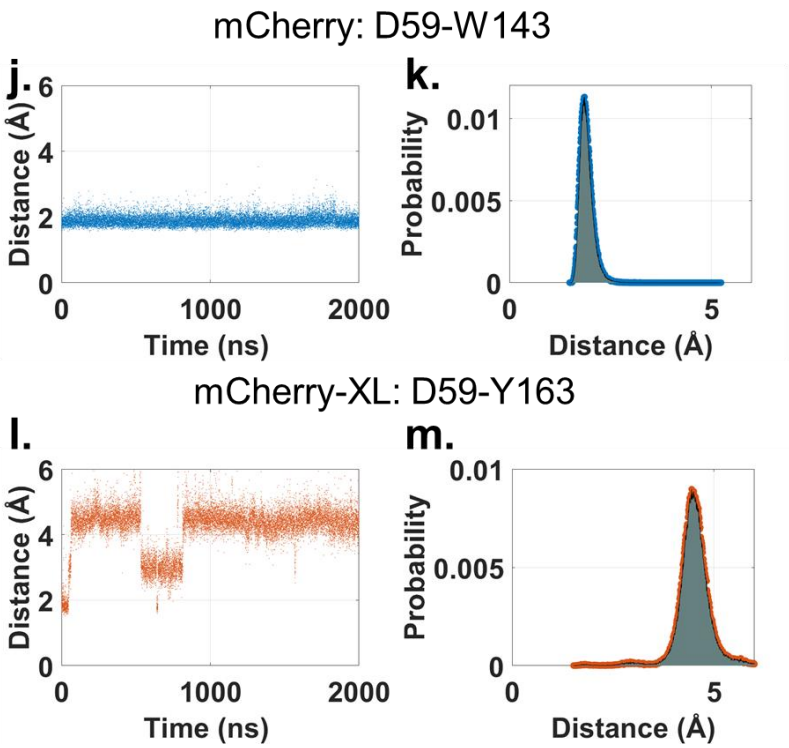

Figure 4: a. The network of interactions between Q163, W143, S62, and D59 and the chromophore in mCherry (PDB ID:2H5Q). (b-m). The distance–time trajectories and the normalized distance histograms for (b-e). 163-chromophore (distances measured for amine H on Q163 on mCherry, phenolic H on Y163 for mCherry-XL and phenol O on CRO), (f-i). 163-143 (distances measured for the amine H on Q163 and the geometric center of the indole moiety on W143 on mCherry, and the O-atom on Y163 and phenolic hydrogen on S143 on mCherry-XL. (j-m) The interaction of the backbone carbonyl O-atom on D59 with the hydrogen of the secondary amine on W143 in mCherry (direct H-bond) and with the phenol of Y163 of mCherry-XL (direct and water-mediated H-bonds).

e. Steric restriction of the chromophore by residue 161

In most mFruit RFPs, the residue at position 161 is aliphatic and does not show any specific long-lived interactions.[55] Because of the sidechain's close proximity to the chromophore's phenol moiety, Campbell and coworkers recognized 161 as a crucial residue for the polarizability of the electron cloud on the FP chromophore.[55] In the variants relevant to this study, barring the exception of C12-8 (I161S), which displays

an effective direct hydrogen-bond between R197 and S161, other variants do not show any specific direct long-lived interaction. However, most FPs in this series do show a weak hydrogen-bonded interaction of the H-atom of the aliphatic residue at this position with the amine residue of K70. We provide the distance histograms identified from our simulations between the residue and the chromophore in the Supplementary Information Figure S9.2.

To further shed light on the role of the 161 sidechain, we experimentally substituted V161 on mCherry-XL to other aliphatic residues, i.e. Ile, Leu, Ala and Gly. Measurements on the purified proteins reveal that larger sidechains such as Leu and Ile, result in red-shifts (λ_{abs}~ 563 nm/ λ_{em}~592 nm) and shorter lifetimes, whereas the smaller amino acids Gly, Ala or Val are blue-shifted (λ_{abs}~ 558 nm/ λ_{em}~587 nm) and generally display longer lifetimes (Supplementary Information Section S9). The longest lifetime of this series is shown by mCherry-XL (~3.9 ns) followed by V161A (~3.6 ns), V161G (~3.4 ns), V161I and V161L (~3 ns; Supplementary Information Section S9). The larger residues, I161 and L161 show similar spectral features and lifetimes, which indicate similar perturbations to the electronic structure of the chromophore due to the comparable size of the Leu and Ile sidechains. However, despite minor spectral changes between V161, A161 and G161 – significant changes in fluorescence lifetime (~0.2 ns) are observed. This establishes the dominant role of sterics that the residue at 161 plays. Though it is possible that the size of the residue at 161 results in a perturbation to the orientation of K70, but the minimal spectral changes indicate otherwise. However, it is interesting to note that despite minimal spectral shifts the increase in lifetime depends on the size of the aliphatic amino acid that fits into this pocket. Additionally, the Stokes shifts observed for larger residues at this position are ~5–10% smaller than for the smaller residues, reflecting the lower reorganization energy from reduced conformational freedom with larger sidechains.

f. Residues directly in contact with oxygen and nitrogen atoms of the chromophore

The crystal structure of mCherry indicates a strong hydrogen bond between the two possible conformers of the hydroxy group on S146 and the phenolate moiety (~2.2 and 2.7 Å) and a single conformation for the R95 sidechain hydrogen bonded to the carbonyl O on the imidazolinone ring (~2 Å) of the chromophore. These residues, which are positioned along the direction of electron flow across the chromophore rings in a S_0–S_1 transition, are critical for the photophysics.[29] This was noted for GFP variants, where the stabilization of the negative charge on the phenolic O-atom was achieved through hydrogen bonds between T203 and the phenolic O, and/or through R96 and the imidazolinone O.[23] Substitutions at these positions resulted in spectral shifts and changes in brightness.[23] Drobizhev and coworkers interpret these changes as results of modulation of electric field strength and directionality across the chromophore along different directions.[29]

Though residues 146 and 95 were not mutated in this study, other mutations acquired on the phenol end of the chromophore clearly influence the dynamics of hydrogen-bonded interactions of S146 and the phenolate moiety of the chromophore. Unlike the crystal structure, we find four major hydrogen-bonded conformers (direct and water mediated; Figure 5) for mCherry variants between the phenolate O of the chromophore and the S146 residue. These conformations are quantified using the distance between the H-atom on the hydroxy group of S146 and the phenolate O on the chromophore. The dominant conformer in mCherry contains an indirect interaction between the N-atom of the peptide linkage of S146 and the phenolate (distance ~6 Å), while the direct hydrogen-bonded conformer, as seen in the crystal structure, dominates the interaction in brighter variants such as mCherry-XL and C12-3 (distance ~2 Å; Supplementary Information Section S11). The other dominant conformers from the simulations also indicate mono- and di-hydrated forms of the phenolate O, hydrogen bonded to S146 through water molecules. The directly hydrogen-bonded conformer of S146 is also qualitatively correlated with the nature of the gap observed for β7- β10 strands, as S146 is located on the floppy β7-strand. Brighter FPs of the mCherry family with a closed β7- β10 gap (mCherry-XL, C12-3, and C12-8) indeed display higher fractions of the directly hydrogen-bonded conformer of S146. (Figures 5 and SI Figure S11.2) In contrast, the imidazolinone end

of the chromophore reveals negligible changes in the hydrogen-bonding patterns with our mutations (R95 and E215; Supplementary Information Section S11). Since no mutations in the course of directed evolution were acquired on the imidazolinone and the acylimine end of the chromophore, the interactions and measured hydrogen-bond distances remain constant. (Supplementary Information Section S11) It is also interesting to note that despite the possible interaction of E215-R197 (SI Table S5.3), the hydrogen bond between the N-atom (N1) on the imidazolinone ring and E215 is minimally perturbed, even for mCherry (I197). These observations corroborate the design strategies proposed by Lin et al. and Drobizhev et al., where brighter variants such as mCherry-XL (and C12-3) seem to exhibit a strong direct hydrogen bond of the phenolate O with residues on the barrel.[23, 29]

Previous hybrid QM-MM simulations on mCherry and mStrawberry revealed that mStrawberry exhibits a floppier structure in comparison to mCherry, as demonstrated by larger backbone fluctuations and the coexistence of two conformers for the sidechain of S146.[56] The production runs for each simulation in this study were short (50 ns), owing to the limitations of the QM-nature of calculations, thereby capturing only two of the four conformations we noted in our simulations. The two conformers reported then correspond to the structures represented in Figures 5b (direct) and 5c (mono-hydrated forms). Additionally, this theoretical study could correctly explain previous pressure dependent fluorescence experiments on red fluorescent proteins TagRFP-S, TagRFP-T, mCherry, mOrange2, mStrawberry, and mKO as a function of pressure up to several GPa, where TagRFP-S, TagRFP-T, mOrange2, and mStrawberry showed an initial increase in fluorescence intensity and spectral blue-shifts upon application of pressure above ambient conditions, and mCherry did not.[57] This indicates that removal of water from the barrel leads to larger fractions of directly H-bonded forms of S146 and the chromophore, which are brighter and blue shifted – further strengthening the model proposed by Lin et al.[23] With 40-fold longer MD-runs in this work, we note the existence of other forms of S146, and more importantly a larger fraction of the directly H-bonded conformer for mCherry-XL, which could further explain the higher brightness and blue-shift observed in this variant.

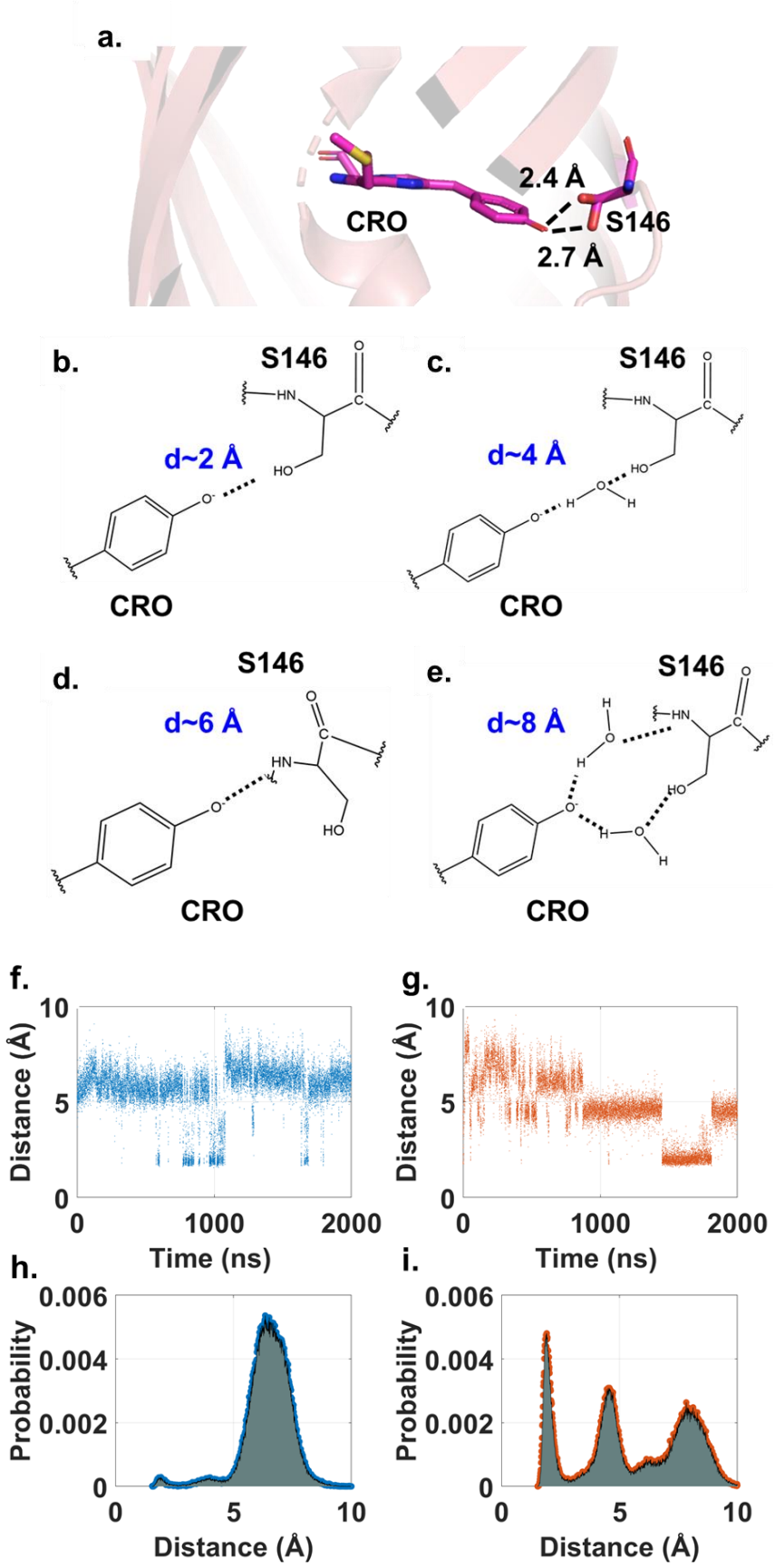
a.
2.4 Å
CRO
S146
2.7 Å
b.
S146
d~2 Å
CRO
c.
S146
d~4 Å
CRO
d.
S146
d~6 Å
CRO
e.
S146
d~8 Å
CRO
f.
Distance (Å)
Time (ns)
g.
Distance (Å)
Time (ns)
h.
Probability
Distance (Å)
i.
Probability
Distance (Å)

Figure 5: a. The two possible conformers of S146 (directly H-bonded to CRO) and the respective distances of the OH group from the crystal structure of mCherry (PDB: 2H5Q) (b-e) The four possible hydrogen-bonded conformers observed for the CRO-S146 interaction in mCherry variants recognized from the MD runs in this work. The distances in blue indicate the spacing between the chromophore phenolate O and the hydroxy group on S146. The four conformers are characterized by (b) a direct hydrogen bond between CRO and S146, (c) a single water mediated hydrogen bond between CRO and S146, (d) a weak hydrogen bond (~3Å) between the phenolate O on the CRO with the backbone N-atom on the peptide linkage of S146, and (e) a double hydrogen bond exhibiting the interactions seen in the forms presented in (c) and (d). (f-i). The distance–time trajectories and normalized histograms of the CRO-S146 interaction in mCherry (blue) and mCherry-XL (orange). In contrast to mCherry, mCherry-XL exhibits long-lived hydrogen-bonded conformers, with a clear presence of the direct hydrogen-bonded conformer in (a) form, consistent with the crystal structure of mCherry.

Conclusions and Outlook

The development of new FPs continues, and new experimentally-determined structures are being added to the Protein Data Bank, along with thousands of new AI-predicted structures which recently appeared in the Alpha-Fold database.[15, 58, 59] Recent advancements on many theoretical and experimental fronts have led to a better understanding of FP photophysics—particularly in the context of the chromophore chemistry.[60 -64] However, there remains a dearth of information when it comes to linking the success of evolving a dim FP to a brighter variant with the underlying structure–function relationships that impact the chromophore photophysics. We followed our previous evolution efforts for mCherry to provide a local analysis of the conformational space in mCherry, mCherry-XL, mScarlet, C12-3, C12-7 and C12-8.[42] One of the notable observations from this study is the crucial role of the substitution I197R, which reduces the barrel flexibility through numerous hydrogen-bonding interactions and introduces an electron-withdrawing moiety that results in the blue-shift of the absorption and emission spectra. Additionally, we observed the disruption of

the Q163-CRO interaction—effectively brightening and blue-shifting mCherry. Finally, we observed the different conformations of S146, which are not visible in low temperature crystal structures, and we could assess the impact of each conformation on the photophysics. By combining the benefits of in-silico simulations and experimental methods, we advance a mechanistic understanding of protein function from a directed evolution effort, providing insight into the functional design of biomarkers that is invaluable to the communities of biophysical chemists, biochemists, and microscopists.

ASSOCIATED CONTENT

Supporting Information: Supplementary Information (Sections S1 to S11) have been provided.

AUTHOR INFORMATION

Corresponding Author

Ralph Jimenez: rjimenez@jila.colorado.edu

Author Contributions

S.M., and R.J. conceptualized the study. R.J., S.M. and P.P.C. designed and analyzed the simulations. S.M., P.M. and N.D. designed and performed the experiments. S.M. and R.J. developed data analysis methods in the study. S.M. and R.J. wrote the manuscript.

Funding Sources

NSF Physics Frontier Center at JILA (PHY 1734006 to R.J.)

Notes

The authors declare no competing financial interest.

ACKNOWLEDGMENTS

S.M. was supported by the NIH/CU Molecular Biophysics Training Program (T32). This work was partially supported by the NSF Physics Frontier Center at JILA (PHY 1734006 to R.J.). R.J. is a member of the Quantum Physics Division of the National Institute of Standards and Technology (NIST). Certain commercial equipment, instruments, or materials are identified in this paper in order to specify the experimental procedure adequately. Such identification is not intended to imply recommendation or endorsement by the NIST, nor is it intended to imply that the materials or equipment identified are necessarily the best available for the purpose. We acknowledge the help of Jim McKown and Eric Alvarado from the JILA Computing facility. Spectroscopy was performed at the W.M. Keck Optical Measurements Laboratory in JILA. We also thank Prof. Amy E. Palmer, Prof. ShengTing Hung, and Kristen Parzuchowski for valuable discussions.

REFERENCES

1. Tsien, R. Y. The Green Fluorescent Protein. *Annu. Rev. Biochem.* **1998**, *67* (1), 509–544. https://doi.org/10.1146/annurev.biochem.67.1.509.

2. Shaner, N. C.; Steinbach, P. A.; Tsien, R. Y. A Guide to Choosing Fluorescent Proteins. *Nat. Methods* **2005**, *2* (12), 905–909. https://doi.org/10.1038/nmeth819.

3. Wu, Y.; Shroff, H. Faster, Sharper, and Deeper: Structured Illumination Microscopy for Biological Imaging. *Nat. Methods* **2018**, *15* (12), 1011–1019. https://doi.org/10.1038/s41592-018-0211-z.

4. Chen, Z.; Truong, T. M.; Ai, H. W. Illuminating Brain Activities with Fluorescent Protein-Based Biosensors. *Chemosensors* **2017**, *5* (4). https://doi.org/10.3390/chemosensors5040032.

5. Chernov, K. G.; Redchuk, T. A.; Omelina, E. S.; Verkhusha, V. V. Near-Infrared Fluorescent Proteins, Biosensors, and Optogenetic Tools Engineered from Phytochromes. *Chem. Rev.* **2017**, *117* (9), 6423–6446. https://doi.org/10.1021/acs.chemrev.6b00700.

6. Espasa, A.; Lang, M.; Aguiño, C. F.; Sanchez-deAlcazar, D.; Fernández-Blázquez, J. P.; Sonnewald, U.; Cortajarena, A. L.; Coto, P. B.; Costa, R. D. Long-Living and Highly Efficient Bio-Hybrid Light-Emitting Diodes with Zero-Thermal-Quenching Biophosphors. *Nat. Commun.* **2020**, *11* (1), 879. https://doi.org/10.1038/s41467-020-14559-8.

7. Leem, J. W.; Jeon, H.-J.; Ji, Y.; Park, S. M.; Kwak, Y.; Park, J.; Kim, K.-Y.; Kim, S.-W.; Kim, Y. L. Edible Matrix Code with Photogenic Silk Proteins. *ACS Cent. Sci.* **2022**, *8* (5), 513–526. https://doi.org/10.1021/acscentsci.1c01233.

8. Campbell, B. C.; Nabel, E. M.; Murdock, M. H.; Lao-Peregrin, C.; Tsoulfas, P.; Blackmore, M. G.; Lee, F. S.; Liston, C.; Morishita, H.; Petsko, G. A. MGreenLantern: A Bright Monomeric Fluorescent Protein with Rapid Expression and Cell Filling Properties for Neuronal Imaging. *Proc. Natl. Acad. Sci. U. S. A.* **2020**, *117* (48), 30710–30721. https://doi.org/10.1073/pnas.2000942117.

9. Mukherjee, S.; Jimenez, R. Photophysical Engineering of Fluorescent Proteins: Accomplishments and Challenges of Physical Chemistry Strategies. *J. Phys. Chem. B* **2022**, *126* (4), 735–750. https://doi.org/10.1021/acs.jpcb.1c05629.

10. Koveal, D.; Rosen, P. C.; Meyer, D. J.; Díaz-García, C. M.; Wang, Y.; Cai, L.-H.; Chou, P. J.; Weitz, D. A.; Yellen, G. A High-Throughput Multiparameter Screen for Accelerated Development and Optimization of Soluble Genetically Encoded Fluorescent Biosensors. *Nat. Commun.* **2022**, *13* (1), 2919. https://doi.org/10.1038/s41467-022-30685-x.

11. Bindels, D. S.; Postma, M.; Haarbosch, L.; van Weeren, L.; Gadella, T. W. J. Multiparameter Screening Method for Developing Optimized Red-Fluorescent Proteins. *Nat. Protoc.* **2020**, *15* (2), 450–478. https://doi.org/10.1038/s41596-019-0250-7.

12. Manna, P.; Hung, S. T.; Mukherjee, S.; Friis, P.; Simpson, D. M.; Lo, M. N.; Palmer, A. E.; Jimenez, R. Directed Evolution of Excited State Lifetime and Brightness in FusionRed Using a Microfluidic Sorter. *Integr. Biol. (United Kingdom)* **2018**, *10* (9), 516–526. https://doi.org/10.1039/c8ib00103k.

13. Dean, K. M.; Davis, L. M.; Lubbeck, J. L.; Manna, P.; Friis, P.; Palmer, A. E.; Jimenez, R. High-Speed Multiparameter Photophysical Analyses of Fluorophore Libraries. *Anal. Chem.* **2015**, *87* (10), 5026–5030. https://doi.org/10.1021/acs.analchem.5b00607.

14. Hung, S. T.; Mukherjee, S.; Jimenez, R. Enrichment of Rare Events Using a Multi-Parameter High Throughput Microfluidic Droplet Sorter. *Lab Chip* **2020**, *20* (4), 834–843. https://doi.org/10.1039/c9lc00790c.

15. Kim, T. Y.; Yoon, T. S.; Kang, S.; Afzal, M. Juggling with Fluorescent Proteins: Spectrum and Structural Changes of the MCardinal2 Variants. *Biochem. Biophys. Res. Commun.* **2022**, *593*, 79–83. https://doi.org/10.1016/j.bbrc.2022.01.044.

16. Julia, D.; F., D. P.; L., P. C.; Michael, E.; C., G. S. Moving beyond the Constraints of Chemistry via Crystal Structure Discovery with Isotropic Multiwell Pair Potentials. *Proc. Natl. Acad. Sci.* **2021**, *118* (21), e2024034118. https://doi.org/10.1073/pnas.2024034118.

17. Fenwick, R. B.; van den Bedem, H.; Fraser, J. S.; Wright, P. E. Integrated Description of Protein Dynamics from Room-Temperature X-Ray Crystallography and NMR. *Proc. Natl. Acad. Sci.* **2014**, *111* (4), E445–E454. https://doi.org/10.1073/pnas.1323440111.

18. Mizuno, H.; Mal, T. K.; Wälchli, M.; Kikuchi, A.; Fukano, T.; Ando, R.; Jeyakanthan, J.; Taka, J.; Shiro, Y.; Ikura, M.; Miyawaki, A. Light-Dependent Regulation of Structural Flexibility in a Photochromic Fluorescent Protein. *Proc. Natl. Acad. Sci. U. S. A.* **2008**, *105* (27), 9227–9232. https://doi.org/10.1073/pnas.0709599105.

19. Polyakov, I. V.; Grigorenko, B. L.; Epifanovsky, E. M.; Krylov, A. I.; Nemukhin, A. V. Potential Energy Landscape of the Electronic States of the GFP Chromophore in Different Protonation Forms: Electronic Transition Energies and Conical Intersections. *J. Chem. Theory Comput.* **2010**, *6* (8), 2377–2387. https://doi.org/10.1021/ct100227k.

20. Bravaya, K. B.; Khrenova, M. G.; Grigorenko, B. L.; Nemukhin, A. V; Krylov, A. I. Effect of Protein Environment on Electronically Excited and Ionized States of the Green Fluorescent Protein Chromophore. *J. Phys. Chem. B* **2011**, *115* (25), 8296–8303. https://doi.org/10.1021/jp2020269.

21. Jones, C. M.; List, N. H.; Martínez, T. J. Steric and Electronic Origins of Fluorescence in GFP and GFP-like Proteins. *J. Am. Chem. Soc.* **2022**, *144* (28), 12732–12746. https://doi.org/10.1021/jacs.2c02946.

22. Romei, M. G.; Lin, C. Y.; Mathews, I. I.; Boxer, S. G. Electrostatic Control of Photoisomerization Pathways in Proteins. *Science (80-.).* **2020**, *367* (6473), 76–79. https://doi.org/10.1126/science.aax1898.

23. Lin, C. Y.; Romei, M. G.; Oltrogge, L. M.; Mathews, I. I.; Boxer, S. G. Unified Model for Photophysical and Electro-Optical Properties of Green Fluorescent Proteins. *J. Am. Chem. Soc.* **2019**, *141* (38), 15250–15265. https://doi.org/10.1021/jacs.9b07152.

24. Dean, K. M.; Lubbeck, J. L.; Binder, J. K.; Schwall, L. R.; Jimenez, R.; Palmer, A. E. Analysis of Red-Fluorescent Proteins Provides Insight into Dark-State Conversion and Photodegradation. *Biophys. J.* **2011**, *101* (4), 961–969. https://doi.org/10.1016/j.bpj.2011.06.055.

25. Acharya, A.; Bogdanov, A. M.; Grigorenko, B. L.; Bravaya, K. B.; Nemukhin, A. V.; Lukyanov, K. A.; Krylov, A. I. Photoinduced Chemistry in Fluorescent Proteins: Curse or Blessing? *Chemical Reviews*. 2017, pp 758–795. https://doi.org/10.1021/acs.chemrev.6b00238.

26. Chang, J.; Romei, M. G.; Boxer, S. G. Structural Evidence of Photoisomerization Pathways in Fluorescent Proteins. *J. Am. Chem. Soc.* **2019**, *141* (39), 15504–15508. https://doi.org/10.1021/jacs.9b08356.

27. Lin, C.-Y.; Romei, M. G.; Mathews, I. I.; Boxer, S. G. Energetic Basis and Design of Enzyme Function Demonstrated Using GFP, an Excited-State Enzyme. *J. Am. Chem. Soc.* **2022**, *144* (9), 3968–3978. https://doi.org/10.1021/jacs.1c12305.

28. Mukherjee, S.; Thomas, C.; Wilson, R.; Simmerman, E.; Hung, S. T.; Jimenez, R. Characterizing Dark State Kinetics and Single Molecule Fluorescence of FusionRed and FusionRed-MQ at Low Irradiances. *Phys. Chem. Chem. Phys.* **2022**. https://doi.org/10.1039/d2cp00889k.

29. Drobizhev, M.; Molina, R. S.; Callis, P. R.; Scott, J. N.; Lambert, G. G.; Salih, A.; Shaner, N. C.; Hughes, T. E. Local Electric Field Controls Fluorescence Quantum Yield of Red and Far-Red Fluorescent Proteins. *Front. Mol. Biosci.* **2021**, *8* (February), 1–21. https://doi.org/10.3389/fmolb.2021.633217.

30. List, N. H.; Jones, C. M.; Martínez, T. J. Internal Conversion of the Anionic GFP Chromophore: In and out of the I-Twisted S_1/S_0 conical Intersection Seam. *Chem. Sci.* **2022**, *13* (2), 373–385. https://doi.org/10.1039/d1sc05849e.

31. Tang, L.; Fang, C. Fluorescence Modulation by Ultrafast Chromophore Twisting Events: Developing a Powerful Toolset for Fluorescent-Protein-Based Imaging. *J. Phys. Chem. B* **2021**, *125* (50), 13610–13623. https://doi.org/10.1021/acs.jpcb.1c08570.

32. Chen, C.; Boulanger, S. A.; Sokolov, A. I.; Baranov, M. S.; Fang, C. A Novel Dialkylamino GFP Chromophore as an Environment-Polarity Sensor Reveals the Role of Twisted Intramolecular Charge Transfer. *Chemosensors.* **2021**, 9, 234. https://doi.org/10.3390/chemosensors9080234.

33. Bindels, D. S.; Haarbosch, L.; Van Weeren, L.; Postma, M.; Wiese, K. E.; Mastop, M.; Aumonier, S.; Gotthard, G.; Royant, A.; Hink, M. A.; Gadella, T. W. J. MScarlet: A Bright Monomeric Red Fluorescent Protein for Cellular Imaging. *Nat. Methods* **2016**, *14* (1), 53–56. https://doi.org/10.1038/nmeth.4074.

34. Bravaya, K. B.; Grigorenko, B. L.; Nemukhin, A. V.; Krylov, A. I. Quantum Chemistry behind Bioimaging: Insights from Ab Initio Studies of Fluorescent Proteins and Their Chromophores. *Acc. Chem. Res.* **2012**, *45* (2), 265–275. https://doi.org/10.1021/ar2001556.

35. Stöhr, M.; Tkatchenko, A. Quantum Mechanics of Proteins in Explicit Water: The Role of Plasmon-like Solute-Solvent Interactions. *Sci. Adv.* **2019**, *5* (12), eaax0024. https://doi.org/10.1126/sciadv.aax0024.

36. Morzan, U. N.; Alonso de Armiño, D. J.; Foglia, N. O.; Ramírez, F.; González Lebrero, M. C.; Scherlis, D. A.; Estrin, D. A. Spectroscopy in Complex Environments from QM–MM Simulations. *Chem. Rev.* **2018**, *118* (7), 4071–4113. https://doi.org/10.1021/acs.chemrev.8b00026.

37. Coppola, F.; Perrella, F.; Petrone, A.; Donati, G.; Rega, N. A Not Obvious Correlation Between the Structure of Green Fluorescent Protein Chromophore Pocket and Hydrogen Bond Dynamics: A Choreography From Ab Initio Molecular Dynamics. *Frontiers in Molecular Biosciences*. 2020. https://doi.org/10.3389/fmolb.2020.569990.

38. Cao, Y.; Romero, J.; Olson, J. P.; Degroote, M.; Johnson, P. D.; Kieferová, M.; Kivlichan, I. D.; Menke, T.; Peropadre, B.; Sawaya, N. P. D.; Sim, S.; Veis, L.; Aspuru-Guzik, A. Quantum Chemistry in the Age of Quantum Computing. *Chem. Rev.* **2019**, *119* (19), 10856–10915. https://doi.org/10.1021/acs.chemrev.8b00803.

39. Sponer, J.; Bussi, G.; Krepl, M.; Banas, P.; Bottaro, S.; Cunha, R. A.; Gil-Ley, A.; Pinamonti, G.; Poblete, S.; Jurečka, P.; Walter, N. G.; Otyepka, M. RNA Structural Dynamics as Captured by Molecular Simulations: A Comprehensive Overview. *Chem. Rev.* **2018**, *118* (8), 4177–4338. https://doi.org/10.1021/acs.chemrev.7b00427.

40. Stone, J. E.; Hardy, D. J.; Ufimtsev, I. S.; Schulten, K. GPU-Accelerated Molecular Modeling Coming of Age. J. Mol. Graph. Model. 2010, 29 (2), 116–125. https://doi.org/10.1016/j.jmgm.2010.06.010.

41. Yelshanskaya, M. V.; Patel, D. S.; Kottke, C. M.; Kurnikova, M. G.; Sobolevsky, A. I. Opening of Glutamate Receptor Channel to Subconductance Levels. *Nature* **2022**, *605* (7908), 172–178. https://doi.org/10.1038/s41586-022-04637-w.

42. Mukherjee, S.; Manna, P.; Hung, S.-T.; Vietmeyer, F.; Friis, P.; Palmer, A. E.; Jimenez, R. Directed Evolution of a Bright Variant of mCherry: Suppression of Nonradiative Decay by Fluorescence Lifetime Selections. *J. Phys. Chem. B* **2022**, *126* (25), 4659–4668. https://doi.org/10.1021/acs.jpcb.2c01956.

43. Mukherjee, S.; Hung, S. T.; Douglas, N.; Manna, P.; Thomas, C.; Ekrem, A.; Palmer, A. E.; Jimenez, R. Engineering of a Brighter Variant of the Fusionred Fluorescent Protein Using Lifetime Flow

Cytometry and Structure-Guided Mutations. *Biochemistry* **2020**, *59* (39), 3669–3682. https://doi.org/10.1021/acs.biochem.0c00484.

44. Phillips, J. C.; Hardy, D. J.; Maia, J. D. C.; Stone, J. E.; Ribeiro, J. V; Bernardi, R. C.; Buch, R.; Fiorin, G.; Hénin, J.; Jiang, W.; McGreevy, R.; Melo, M. C. R.; Radak, B. K.; Skeel, R. D.; Singharoy, A.; Wang, Y.; Roux, B.; Aksimentiev, A.; Luthey-Schulten, Z.; Kalé, L. V; Schulten, K.; Chipot, C.; Tajkhorshid, E. Scalable Molecular Dynamics on CPU and GPU Architectures with NAMD. *J. Chem. Phys.* **2020**, *153* (4), 44130. https://doi.org/10.1063/5.0014475.

45. Phillips, J. C.; Braun, R.; Wang, W.; Gumbart, J.; Tajkhorshid, E.; Villa, E.; Chipot, C.; Skeel, R. D.; Kalé, L.; Schulten, K. Scalable Molecular Dynamics with NAMD. *J. Comput. Chem.* **2005**, *26* (16), 1781–1802. https://doi.org/10.1002/jcc.20289.

46. Humphrey, W.; Dalke, A.; Schulten, K. VMD: Visual Molecular Dynamics. *J. Mol. Graph.* **1996**, *14* (1), 33–38. https://doi.org/10.1016/0263-7855(96)00018-5.

47. Chapagain, P. P.; Regmi, C. K.; Castillo, W. Fluorescent Protein Barrel Fluctuations and Oxygen Diffusion Pathways in MCherry. *J. Chem. Phys.* **2011**, *135* (23), 235101. https://doi.org/10.1063/1.3660197.

48. Regmi, C. K.; Bhandari, Y. R.; Gerstman, B. S.; Chapagain, P. P. Exploring the Diffusion of Molecular Oxygen in the Red Fluorescent Protein MCherry Using Explicit Oxygen Molecular Dynamics Simulations. *J. Phys. Chem. B* **2013**, *117* (8), 2247–2253. https://doi.org/10.1021/jp308366y.

49. Perri, A.; Gaida, J. H.; Farina, A.; Preda, F.; Viola, D.; Ballottari, M.; Hauer, J.; De Silvestri, S.; D'Andrea, C.; Cerullo, G.; Polli, D. Time- and Frequency-Resolved Fluorescence with a Single TCSPC Detector via a Fourier-Transform Approach. *Opt. Express* **2018**, *26* (3), 2270–2279. https://doi.org/10.1364/OE.26.002270.

50. Dean, K. M.; Lubbeck, J. L.; Davis, L. M.; Regmi, C. K.; Chapagain, P. P.; Gerstman, B. S.; Jimenez, R.; Palmer, A. E. Microfluidics-Based Selection of Red-Fluorescent Proteins with Decreased Rates of Photobleaching. *Integr. Biol. (United Kingdom)* **2015**, *7* (2), 263–273. https://doi.org/10.1039/c4ib00251b.

51. Shu, X.; Shaner, N. C.; Yarbrough, C. A.; Tsien, R. Y.; Remington, S. J. Novel Chromophores and Buried Charges Control Color in MFruits. *Biochemistry* **2006**, *45* (32), 9639–9647. https://doi.org/10.1021/bi060773l.

52. Bravaya, K. B.; Subach, O. M.; Korovina, N.; Verkhusha, V. V.; Krylov, A. I. Insight into the Common Mechanism of the Chromophore Formation in the Red Fluorescent Proteins: The Elusive Blue Intermediate Revealed. *J. Am. Chem. Soc.* **2012**, *134* (5), 2807–2814. https://doi.org/10.1021/ja2114568.

53. Shaner, N. C.; Campbell, R. E.; Steinbach, P. A.; Giepmans, B. N. G.; Palmer, A. E.; Tsien, R. Y. Improved Monomeric Red, Orange and Yellow Fluorescent Proteins Derived from Discosoma Sp. Red Fluorescent Protein. *Nat. Biotechnol.* **2004**, *22* (12), 1567–1572. https://doi.org/10.1038/nbt1037.

54. Chica, R. A.; Moore, M. M.; Allen, B. D.; Mayo, S. L. Generation of Longer Emission Wavelength Red Fluorescent Proteins Using Computationally Designed Libraries. *Proc. Natl. Acad. Sci. U. S. A.* **2010**, *107* (47), 20257–20262. https://doi.org/10.1073/pnas.1013910107.

55. Campbell, R. E.; Tour, O.; Palmer, A. E.; Steinbach, P. A.; Baird, G. S.; Zacharias, D. A.; Tsien, R. Y. A Monomeric Red Fluorescent Protein. *Proc. Natl. Acad. Sci. U. S. A.* **2002**, *99* (12), 7877–7882. https://doi.org/10.1073/pnas.082243699.

56. Laurent, A. D.; Mironov, V. A.; Chapagain, P. P.; Nemukhin, A. V.; Krylov, A. I. Exploring Structural and Optical Properties of Fluorescent Proteins by Squeezing: Modeling High-Pressure Effects on the Mstrawberry and Mcherry Red Fluorescent Proteins. *J. Phys. Chem. B* **2012**, *116* (41), 12426–12440. https://doi.org/10.1021/jp3060944.

57. Pozzi, E. A.; Schwall, L. R.; Jimenez, R.; Weber, J. M. Pressure-Induced Changes in the Fluorescence Behavior of Red Fluorescent Proteins. *J. Phys. Chem. B* **2012**, *116* (34), 10311–10316. https://doi.org/10.1021/jp306093h.

58. Muslinkina, L.; Pletnev, V. Z.; Pletneva, N. V.; Ruchkin, D. A.; Kolesov, D. V.; Bogdanov, A. M.; Kost, L. A.; Rakitina, T. V.; Agapova, Y. K.; Shemyakina, I. I.; Chudakov, D. M.; Pletnev, S. Two Independent Routes of Post-Translational Chemistry in Fluorescent Protein FusionRed. *Int. J. Biol. Macromol.* **2020**, *155*, 551–559. https://doi.org/10.1016/j.ijbiomac.2020.03.244.

59. Jumper, J.; Evans, R.; Pritzel, A.; Green, T.; Figurnov, M.; Ronneberger, O.; Tunyasuvunakool, K.; Bates, R.; Žídek, A.; Potapenko, A.; Bridgland, A.; Meyer, C.; Kohl, S. A. A.; Ballard, A. J.; Cowie, A.; Romera-Paredes, B.; Nikolov, S.; Jain, R.; Adler, J.; Back, T.; Petersen, S.; Reiman, D.; Clancy, E.; Zielinski, M.; Steinegger, M.; Pacholska, M.; Berghammer, T.; Bodenstein, S.; Silver, D.; Vinyals, O.; Senior, A. W.; Kavukcuoglu, K.; Kohli, P.; Hassabis, D. Highly Accurate Protein Structure Prediction with AlphaFold. *Nature* **2021**, *596* (7873), 583–589. https://doi.org/10.1038/s41586-021-03819-2.

60. Zagorec-Marks, W.; Foreman, M. M.; Verlet, J. R. R.; Weber, J. M. Probing the Microsolvation Environment of the Green Fluorescent Protein Chromophore in Vacuo. *J. Phys. Chem. Lett.* **2020**, *11* (5), 1940–1946. https://doi.org/10.1021/acs.jpclett.0c00105.

62. Moron, V.; Marazzi, M.; Wanko, M. Far Red Fluorescent Proteins: Where Is the Limit of the Acylimine Chromophore? *J. Chem. Theory Comput.* **2019**. https://doi.org/10.1021/acs.jctc.9b00070.

63. Lyu, T.; Sohn, S. H.; Jimenez, R.; Joo, T. Temperature-Dependent Fluorescence of mPlum Fluorescent Protein from 295 to 20 K. *J. Phys. Chem. B* **2022**, *126* (12), 2337–2344. https://doi.org/10.1021/acs.jpcb.1c10516.

64. De Zitter, E.; Ridard, J.; Thédié, D.; Adam, V.; Lévy, B.; Byrdin, M.; Gotthard, G.; Van Meervelt, L.; Dedecker, P.; Demachy, I.; Bourgeois, D. Mechanistic Investigations of Green MEos4b Reveal a Dynamic Long-Lived Dark State. *J. Am. Chem. Soc.* **2020**, *142* (25), 10978–10988. https://doi.org/10.1021/jacs.0c01880.

For Table of Contents use only